Research Article | Vol. 28, No. 7 / 30 March 2020 / Optics Express 10062
Optics EXPRESS

Sampling moiré method: a tool for sensing quadratic phase distortion and its correction for accurate quantitative phase microscopy

NIKHIL JAYAKUMAR,[1,3] AZEEM AHMAD,[1,3,4] DALIP SINGH MEHTA,[2] AND BALPREET SINGH AHLUWALIA[1,5]

[1]Department of Physics and Technology, UiT The Arctic University of Norway, Tromsø 9037, Norway
[2]Department of Physics, Indian Institute of Technology Delhi, Hauz Khas, New Delhi 110016, India
[3]These authors contributed equally to this work
[4]ahmadazeem870@gmail.com
[5]balpreet.singh.ahluwalia@uit.no

Abstract: The advantages of quantitative phase microscopy (QPM) such as label-free imaging with high spatial sensitivity, live cell compatibility and high-speed imaging makes it viable for various biological applications. The measurement accuracy of QPM strongly relies on the shape of the recorded interferograms, whether straight or curved fringes are recorded during the data acquisition. Moreover, for a single shot phase recovery high fringe density is required. The wavefront curvature for the high-density fringes over the entire field of view is difficult to be discerned with the naked eye. As a consequence, there is a quadratic phase aberration in the recovered phase images due to curvature mismatch. In the present work, we have implemented sampling moiré method for real-time sensing of the wavefront curvature mismatch between the object and the reference wavefronts and further for its correction. By zooming out the interferogram, moiré fringes are generated which helps to easily identify the curvature of the fringes. The wavefront curvature mismatch correction accuracy of the method is tested with the help of low temporal coherent light source such as a white light (temporal coherence ~ 1.6 μm). The proposed scheme is successfully demonstrated to remove the quadratic phase aberration caused due to wavefront mismatch from an USAF resolution target and the biological tissue samples. The phase recovery accuracy of the current scheme is further compared with and found to better than the standard method called principle component analysis. The proposed method enables recording of the corrected wavefront interferogram without needing any additional optical components or modification and also does not need any post-processing correction algorithms. The proposed method of curvature compensation paves the path for a high-throughput and accurate quantitative phase imaging.

1. Introduction

Quantitative phase microscopy (QPM) is a label-free optical technique and within life sciences is primarily used for cell and tissue imaging, such as diagnosis of prostate cancer [1,2], quantifying biophysical parameters like cell membrane fluctuations, dry mass density of cells [1], and other parameters. The main drivers of QPM techniques in biology are quantification of optical thickness with a sub-wavelength accuracy and label-free imaging at a high-speed for the dynamic specimens. To quantify the parameters of interest, a phase map of the object under study has to be generated. For extracting phase map, the light scattered by the specimen and the reference beam, both derived from the same source, are interfered. The interferogram captured by the camera contains both the amplitude and the phase information of the specimen. The phase map of the specimen can then be numerically reconstructed from the interference fringes.

#383461 https://doi.org/10.1364/OE.383461
Journal © 2020 Received 15 Nov 2019; revised 9 Feb 2020; accepted 11 Feb 2020; published 24 Mar 2020

Optics EXPRESS

High-throughput, i.e. high-speed imaging over large field-of-view (FoV), with high sensitivity are desirable in QPM to capture fast events happening inside the biological specimens. QPM can be implemented in either in-line or off-axis geometries and the phase recovery can be performed by either a phase shifting [3–7] or a Fourier transform methods [8–10], respectively. Off-axis geometry implemented with Fourier transform method enables single-shot QPM, offering high-speed imaging over large field-of-view, which together delivers high-throughput imaging as relevant for live cell imaging [1,9,11,12]. However, for a lossless reconstruction of the object, the zero and the first order peaks in the Fourier domain are to be well separated, which mandates a high density of fringes.

Mostly QPM systems suffer from the aberration caused due to curvature mismatch between the object and the reference wavefronts. Therefore, complete compensation of aberrations in the optical system is mandatory for precise phase recovery of the specimen. In an off-axis arrangement, there are mainly two reasons for phase aberration, firstly, the angle between the reference and the object beam introduces a first-order phase distortion and, secondly, the use of a microscope objective (MO) introduces a quadratic phase distortion [13]. The first order phase distortion can be easily compensated by shifting the first order Fourier peak to the origin [1,9]. However, for quadratic phase distortion removal, both the physical [14] and the numerical [15] methods have been developed in the past.

It has been reported that a non-telecentric QPI system [16] introduces a parabolic phase perturbation at the image plane. The natural way to compensate for these errors is through the use of a telecentric imaging system. However, realizing this condition in an off-axis geometry is difficult due to the presence of high-density fringes over the entire FoV of the camera. Dobas *et al.* [17] proposed the use of an electrically controlled liquid lens to produce a spherical wavefront, depending on the microscope objective used, to cancel out the phase perturbation at the image plane. Ferraro *et al.* [18] described a numerical posteriori procedure – a double exposure method in which the phase map reconstructed from a reference calibration hologram (without the object) is subtracted from the phase map reconstructed from the hologram containing the object. However, these physical methods require the modification of the existing setup or are limited in temporal resolution due to the need for recording of multiple frames and also often depend on post-processing of the image. In [16], the spherical curvature in the object beam is compensated through an in-line geometry setup, by introducing the same physical curvature in the reference beam. However, this method of observing the Fourier spectra of the recorded hologram to ascertain phase errors may fail and leave phase residual error. Post processing numerical methods such as 2D Zernike polynomial fitting [19], phase mask method by Ferraro *et al.* [18], phase aberration compensation using principal component analysis [20,21], least square fitting technique [22] etc. are also employed for phase error compensation. In [23], a phase mask, the parameters of which are generated via phase gradient fitting and optimization, is subtracted from the acquired data for a phase curvature compensation. Recently, Nguyen *et al.* employed deep learning by combining convolutional neural network with Zernike polynomial fitting to automatically compensate for phase aberrations in real time [24]. However, the deep-learning approaches requires training of the system which besides being time-consuming process is usually system and application specific.

In this article, we propose a real-time, simple and effective physical technique for off-axis interferometry to eliminate quadrating phase errors arising from wavefront mismatch due to improper optical alignment. The present work does not deal with other optical aberrations, like chromatic and monochromatic aberrations, caused due to the optical system. However, the presence of other optical aberrations in the system can also be discerned using fringes, which is not the scope of this article. In the off-axis setup, the shape of the high fringe density in the interferograms over the entire FoV of the camera cannot be well discerned by a naked human eye which is a low pass filter. To make the shape of the fringes visible to a naked human eye, the

Optics EXPRESS

concept of sampling moiré method is utilized. When the high-density interferogram is displayed on a pixelated computer monitor at different magnifications – the image will be sampled by different number of the monitor pixels. This enables the high frequency information of the interferogram to be converted into a lower frequency and thereby, allows the naked human eye to discern the shape of the fringes. In other words, any slight deviation in the interferogram becomes visible to human eye in the under-sampled signal due to the generation of moiré patterns. The deviations introduced due to optical path length mismatch can be compensated by adjusting the reference arm before recording the interferograms. It is demonstrated both numerically and experimentally that the proposed method of using moiré fringes can be easily implemented for accurate phase reconstruction. The feasibility of phase reconstruction using the concept of moiré fringes is demonstrated on biological tissue sample as well as on an USAF chart.

2. Materials and method

2.1. Basic theory of QPM

The intensity distribution of the interference pattern due to object wave $O_{(x,y)}$ and a reference plane wave $R_{(x,y)} = R_{0(x,y)}e^{i2\pi f_R x}$, where $f_R = \frac{\sin\theta}{\lambda}$,at the plane of CCD can be written as [9,25]:

$$I_{(x,y)} = |R_{(x,y)}|^2 + |O_{(x,y)}|^2 + O^*_{(x,y)}R_{(x,y)} + R^*_{(x,y)}O_{(x,y)} \tag{1}$$

where $O^*_{(x,y)}$ and $R^*_{(x,y)}$ represent the complex conjugates of the object and reference wave respectively. Then $a_{(x,y)} = |R_{(x,y)}|^2 + |O_{(x,y)}|^2$, represents a band limited signal centered around the zero frequency, also known as the dc term. If the band width of the object wave along the x-axis of the Fourier plane is taken as 2B, then the bandwidth of the dc term is 4B. Equation (1) may be modified as shown below.

$$I_{(x,y)} = a_{(x,y)} + b_{(x,y)}\cos[2\pi f_R x - \varphi_{(x,y)}] \tag{2}$$

where $b_{(x,y)} = 2|R_{(x,y)}||O_{(x,y)}|$ and $\varphi_{(x,y)}$ is the argument of the function $O_{(x,y)}$. The Fourier transform of Eq. (2) will generate three main lobes - Fourier transform of $a_{(x,y)}$ will be located near the zero frequency and Fourier transform of the cosine function will generate two peaks at $(f_R, 0)$ and $(-f_R, 0)$. For a faithful reconstruction the central dc term should not overlap with the +1 order or -1 order peaks. Mathematically it means that $f_R = \frac{\sin\theta}{\lambda} \geq 3B$. It implies that θ should be chosen to be greater than a certain minimum value. This will result in a high density of fringes as fringe period is inversely proportional to θ.

2.2. Sampling moiré effects

The classical sampling theorem states that the information contained in a continuous signal f(x) can be faithfully reconstructed from its sampled version $f(x_k)$ if the sampling frequency f_s satisfies the Nyquist sampling criteria, i.e., f_s is atleast twice the highest frequency contained in f(x). When this condition is not satisfied, moiré or aliasing effects start becoming visible. Now, when a digital image is displayed on a monitor, interaction between a periodic signal (pixelated image) and the periodic sampling process (pixelated monitor) takes place and as a result sampled moiré patterns or sub-Nyquist artefacts may arise [26]. A detailed mathematical analysis of the sampling moiré is presented by Issac Amidror [26] and the variety of applications where moiré fringes are employed are presented in [27].

Numerous applications involving moiré fringes have evolved over the years. Moiré fringes based on Talbot effect are employed to generate collimated beams [28,29]. The technique of sampling moiré finds applications in displacement measurements in material science as it provides better resolution at high-speed [30]. Li *et al.* proposed a nanoscale sensitive 3D scanning electron microscope moiré method for 3D shape measurement [31]. Patorski *et al.* enhanced the

Optics EXPRESS

displacement sensitivity of atomic force microscopy by utilizing the higher harmonics of the superposing structures [32].

When a signal with a frequency f is sampled at f_s, then the frequency f_m of the sampling moiré pattern is given by (when $f_s \approx f$):

$$f_m = |f_s - f| \tag{3}$$

It implies that the sampled moiré pattern is generated with a new false lower frequency f_m and becomes conspicuous even with the naked eye due to its magnified period. This concept of sampling is illustrated by the simplified one-dimensional case shown in Fig. 1.

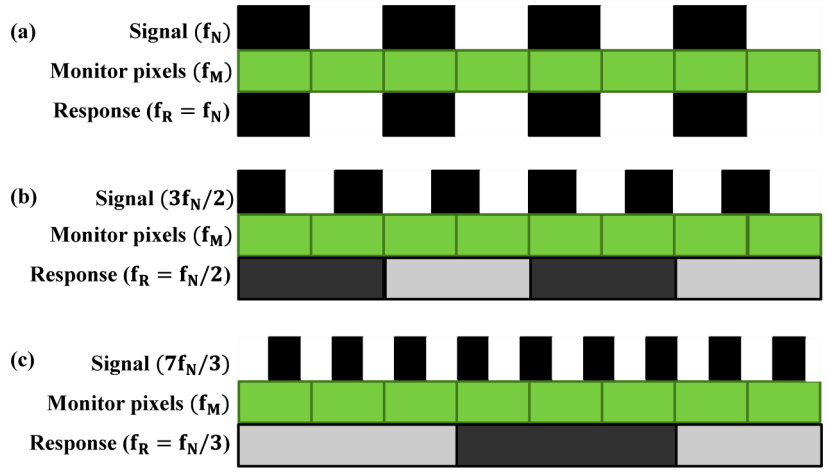

Fig. 1. Schematic representation of an image recorded by the camera getting sampled by the workstation monitor. Black and white colors represent gray values 0 and 255 respectively. Other colors represent intermediate gray values. The gray value in the response signal is the average intensity value registered on a given pixel of the monitor.

To understand the concept of moiré, square waves with different spatial frequencies are considered and sampled at a rate Δx_M (monitor pixel size) as illustrated in Fig. 1. The frequency $f_M = {}^{1}/_{\Delta x_M}$ is called the spatial frequency of monitor pixels. In Fig. 1(a), the square wave (signal) has a spatial frequency 'f_N' equal to half of the pixel frequency of the monitor (f_M). This satisfies the Nyquist condition and as a result the bright and dark regions of the square wave get displayed by each monitor's pixels without any loss of information. This is termed as Response in Fig. 1. It has a spatial frequency f_N and is the exact replica of the square wave, i.e., no aliasing effects are observed. Figures 1(b) and 1(c) represent the cases where Nyquist criteria is not satisfied. In Figs. 1(b) and 1(c), the square waves have spatial frequencies $3f_N/2$ and $7f_N/3$, respectively. The corresponding spatial frequencies of the response signal are found to be equal to $f_N/2$ and $f_N/3$, respectively, which are less than the original signal frequencies. This is due to the under sampling of the signal by the monitor's pixels and leads to the formation of moiré pattern.

The simulation presents the superposition of the interferograms having different fringe shapes and periodic pixel patterns in the computer display as illustrated in Fig. 2. The interference fringes are simulated for different optical path differences (OPDs) between the two interfering beams called object and reference waves. The straight line fringes are formed if the curvatures of both the wavefronts are matched. Any deviation from the wavefront matched condition leads to the formation of curved fringes and resulting in an unwanted spherical phase. Figures 2(a) – 2(c) depict the simulations of interference patterns with negative, zero and positive OPDs between the wavefronts, respectively. Figures 2(a_1)–2(c_1) show the zoomed views of the region of interest enclosed within the yellow dotted box. It is difficult to visualize the shape of the fringes from the

Optics EXPRESS

actual or zoomed images. However, the reconstructed phase maps presented in Figs. 2(d)–2(f) clearly show different phase profiles corresponding to the simulated interferograms shown in Figs. 2(a)–2(c). Therefore, one would need to reconstruct the phase map from the interferogram to know whether complete compensation of the unwanted spherical phase is accomplished or not. On the contrary, when a high fringe density interferogram is demagnified and displayed on a computer screen, the shape of the fringes in the interferogram is easily discerned in the corresponding moiré patterns as shown in Figs. 2(a_2)–2(c_2). Demagnification of the interferogram varies the number of fringes registered on a given pixel of the display and leads to the formation of moiré fringes as explained in Fig. 1. To generate moiré patterns, the interferograms are displayed at 6% magnification using MATLAB. The concept of moiré pattern is further implemented for aberration compensation from the phase images before the data acquisition.

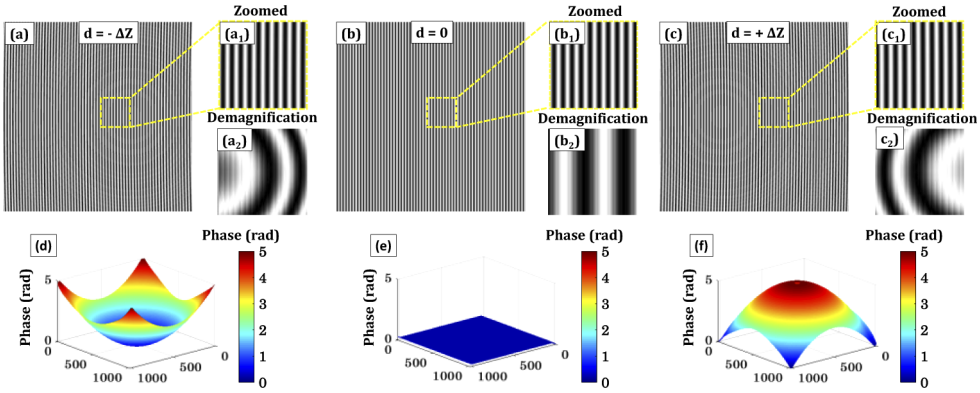

Fig. 2. Simulation study for the sensing of wavefront curvature mismatch using moiré effect. Simulated off-axis high fringe density interferograms generated due to mismatched/matched object and reference wavefront curvatures. (a – c) Simulated interferograms due to superposition of object and reference beam coming from two point sources separated by a distance – ΔZ, 0, + ΔZ, respectively. (a_1 – c_1) Zoomed view of the interferograms marked with yellow dotted box shown in Figs. 2(a)–2(c). (a_2 – c_2) Demagnification of the interferograms illustrated in Figs. 2(a)–2(c) to generate moiré patterns due to the superposition of zoomed out simulated interferograms and workstation monitor pixel pattern for the sensing of wavefront curvature mismatch. (d – f) Reconstructed phase maps corresponding to the interferograms depicted in Figs. 2(a)–2(c). Color map shows phase values in radian.

3. Simulation study

3.1. *Moiré pattern due to the superposition of interferogram and computer screen pixels pattern*

The specifications of the CMOS camera and the workstation monitor given in Table 1 are used for the simulation studies. The length of the simulated interferogram is considered to be equal to the effective sensing area of the CMOS sensor 'L_{Int}'. The effective number of pixels 'N_{Int}' in the interferogram are considered to be equal to 2048 (H) × 2048 (V). Therefore, the pixel size 'Δx_{Int}' of the interferogram is $\Delta x_{Int} = {}^{L_{Int}}/_{N_{Int}} = 6.5$ μm. The pixel size of the computer monitor 'Δx_M' being used to display the interferogram is $\Delta x_M = 270$ μm. There is a difference between the pixel size of the sensor and computer monitor. Therefore, if it is considered that one pixel of the camera is displayed on one pixel of the monitor, then, the additional magnification 'M' due to the pixel size difference is defined as follows:

$$M = \frac{\Delta x_M}{\Delta x_{Int}} = \frac{270\ \mu m}{6.5\ \mu m} \approx 41.53$$

Optics EXPRESS

It means that the image captured on the sensor chip is magnified by 41.53 times while being displayed on the workstation monitor. In simulation studies, the fringe period of the interferogram is kept 9 camera pixels (same as the experimentally recorded interferogram), i.e., $NP_{fringe} = 9$.

Table 1. Technical specifications of the CMOS camera and the workstation monitor used for simulation study

Specification	Camera	Workstation monitor
Model #	Hamamatsu C11440-42U30	Philips 240B4QPYEB/00
Number of pixels 'N'	2048 (H) × 2048 (V)	1920 (H) × 1200 (V)
Pixel size 'Δx'	6.5 μm × 6.5 μm	270 μm × 270 μm
Effective pixel area 'L'	13.312 mm × 13.312 mm	518.4 mm × 324 mm

Total number of fringes over the length of the simulated interferogram,

$$NT_{fringe} = \frac{L_{Int}}{(NP_{fringe} \times \Delta x_{Int})} \tag{4}$$

The simulated interferogram can be displayed at different magnifications (M_{disp}) to generate different moiré fringe patterns. The total number of pixels of the monitor used to display the simulated interferogram can be calculated as follows:

$$NT_M = (L_{Int} \times M \times M_{disp})/\Delta x_M \tag{5}$$

From Eq. (5), the interferogram of 2048 × 2048 pixels, displayed at a magnification of 1% of its actual size, will use 20 × 20 pixels of the monitor. As the total number of fringes over the length of the simulated interferogram are approximately equal to 227.55 (from Eq. (4)). Therefore, each pixel of the monitor will display the average of approximately 11.3 fringes and leads to the formation of moiré fringes as described in Fig. 3. The moiré pattern, which naturally has a low frequency, is generated as a consequence of under-sampling of the image and helps in deciding the shape of the fringes of the interferogram. Similar moiré effect will also be observed for other magnification levels from 2% – 21% as illustrated in Fig. 3. At 21% display magnification, single fringe will be displayed on 2 pixels of the display and satisfy the Nyquist sampling criteria. Thus, the interferogram display magnifications more than 21% will not generate any moiré patterns. The effect of the phase shift in the original interferogram on the moiré pattern is also studied. It is observed that the shift in the fringe pattern does not change the shape of the moiré pattern. It only shifts the moiré pattern as depicted in the bottom row of Fig. 3.

3.2. Experimental setup

The schematic of QPM system based on Linnik interferometer is shown in Fig. 4. Light from a continuous laser source is passed through a rotating diffuser RD to reduce speckle noise by destroying its spatial coherence [4,10,33–35]. The output from the RD is coupled into a multi-mode fiber bundle (MMFB) placed at 1 mm away from the diffuser. The size of the spatially incoherent light exiting the MMFB is controlled and kept equal to 1 mm using a variable aperture A. The output of MMFB is nearly collimated by using lens L_1 (FL: 75 mm) and further focused onto the back focal planes of the microscope objectives MO_2 (10×/0.25 NA) and MO_3 (10×/0.25 NA) using lens L_2 (FL: 125 mm) and 50:50 beam splitter BS. MO_2 and MO_3 send nearly collimated light towards the sample and reference mirror, respectively. The light is reflected from the sample and the reference mirror and is collected again by same objective lenses to further recombine at BS. The object and reference wave are collected by lens L_3 (FL: 200 mm) and superimpose at the camera plane to form interference patterns. The interferogram is recorded using CMOS camera (Hamamatsu C11440 ORCA-Flash 4.0 LT) and further displayed on a

Optics EXPRESS

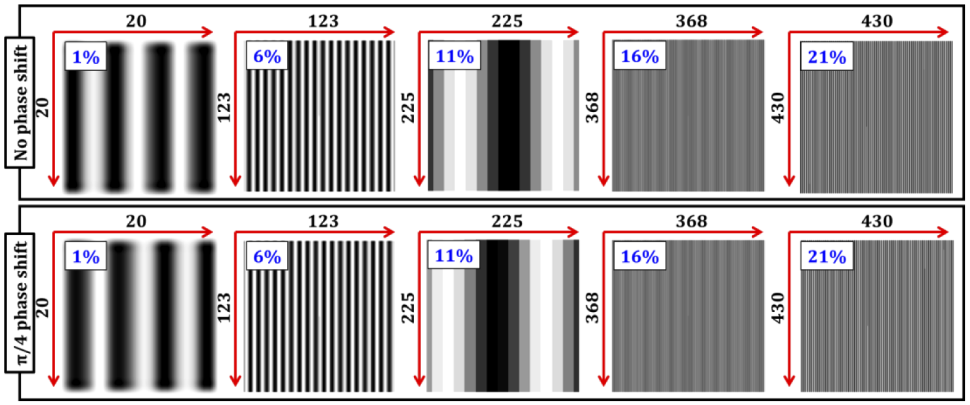

Fig. 3. Simulation results for under sampling of the interferogram recorded by the CMOS camera by the workstation monitor for different magnifications. The top and bottom row represents two different signals shifted in phase by pi/4 radians. From left to right, the images are displayed at different magnification levels 1%, 6%, 11%, 16% and 21% of the original size. The change in display magnification changes the interferogram's frequency displayed on the monitor and leads to the generation of moiré patterns.

monitor (Philips 240B4QPYEB/00). The details of the camera and monitor are given in Section 3.1. The magnification and demagnification of the interferograms are done using the camera software before capturing or storing them in the computer.

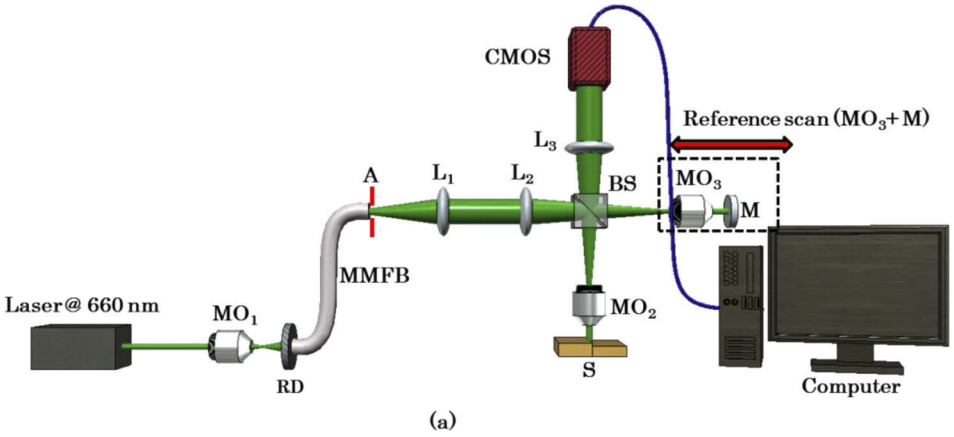

Fig. 4. Schematic diagram of the QPM system. MO_{1-3}: Microscope objectives; BS: Beam splitter; L_{1-3}: Lenses; RD: Rotating diffuser; MMFB: Multiple multi-mode fiber bundle; SMF: Single mode fiber; A: Aperture; M: Mirror and CMOS: Complementary metal oxide semiconductor camera.

4. Results and discussion

4.1. Wavefront curvature mismatch sensing using the concept of moiré pattern

In this section, experimental validity of the simulation studies is demonstrated. Figure 5(a) depicts a screen shot of the camera software. Figures 5(b) and 5(c) are the zoomed in regions of the red and blue dotted boxes in Fig. 5(a). Two identical MOs (MO_2 and MO_3) are used for generating the interferogram. Figures 5(d)–5(f) show the high frequency interferograms

Optics EXPRESS

for optical path length differences of $d_0 - 500$ μm, d_0 μm, $d_0 + 500$ μm, respectively, where d_0 represents the distance at which the optical path lengths of both the arms of the interferometer are matched. The OPD change between the object and the reference arms is done by translating the reference objective MO_3 and the mirror simultaneously (Fig. 4). Figure 5(h) represents a flat phase profile, and since no object is involved it may be considered as the system phase. At d_0 the curvatures of wavefronts in both the interferometer arms are matched and straight fringes are generated. The straight line fringes only generate first order phase aberration in the recovered phase images which can be easily compensated by shifting the first order Fourier peak to the origin of frequency domain [9]. The straight line fringe formation requires equal distance between the reference mirror to the detector plane and the sample substrate to the detector plane. Any deviation from this condition results in a spherical phase getting erroneously added into the recovered phase images.

It becomes difficult to differentiate between the recorded interferograms corresponding to different OPD positions when interferograms are displayed at their actual size as shown in Figs. 5(d)–5(f). This can be understood by looking at the zoomed view of the fringes enclosed by dotted yellow boxes. However, their corresponding phase maps illustrate an error of almost 3 rad when the reference arm is translated by ±500 μm from zero OPD condition. The insets in red dotted boxes depict the moiré fringe patterns at an initial magnification of 6%. It can be seen that the interferograms corresponding to the three different cases of OPD generate different moiré patterns. Insets in Figs. 5(d) and 5(f) represent the wavefront curvature mismatch condition as curved fringes are observed in the moiré patterns. The recovered phase maps corresponding to the recorded interferograms are depicted in Figs. 5(g)–5(i). Figure 5(h) illustrates an almost flat phase profile which corresponds to the straight line moiré pattern. Thus, the proposed method works well for sensing and correction of a wavefront curvature mismatch.

The moiré fringes can also be generated online easily using LabView framework by overlapping the fringe pattern with digitally generated reference structure. This is called digital moiré principle. This can be another option for the judgment of the shape of interference patterns. Moreover, the proposed sampling moiré approach is not only limited to either vertical or horizontal fringes. It can also be used with any orientation of the interference fringes and consequently be used to control the orientation angle of the interference fringes accurately.

4.2. *Wavefront curvature mismatch measurement accuracy*

It has been demonstrated in the previous section that moiré method for wavefront curvature mismatch compensation works well. A piece of standard silicon wafer (flatness < 1 μm, roughness < 1 nm) is used in both the arms of the interferometer (Fig. 4) to generate good contrast interferograms. Before measuring the accuracy of the method, a white light source having low temporal coherence length (~ 1.6 μm) is utilized in the interferometer to decide the reference arm step size for the experiments. The reference mirror is kept at a high angle with respect to the vertical to generate the high fringe density interferograms for single shot phase retrieval. Therefore, confinement of the white light fringes would be in a limited region of the camera FoV. For a particular tilt position of the reference mirror during the experiments, first, reference arm of the interferometer is positioned in a way such that the white light interferogram is observed at one extreme end of the camera FoV. Then the reference arm is translated in steps of 5 μm until the white light fringe shifts to the other end of the camera FoV. The shifting of the white light fringe from one end to other end of the camera FoV covers 50 μm translation of the reference arm. Thus, the step size of 50 μm would be sufficient for further experiments and is determined by observing the movement of white light fringes across the field of view (see Visualization 1). In other words, an error of 50 μm in determining the position of reference arm for straight moiré fringes does not lead to the generation of significant quadratic phase aberration.

Optics EXPRESS

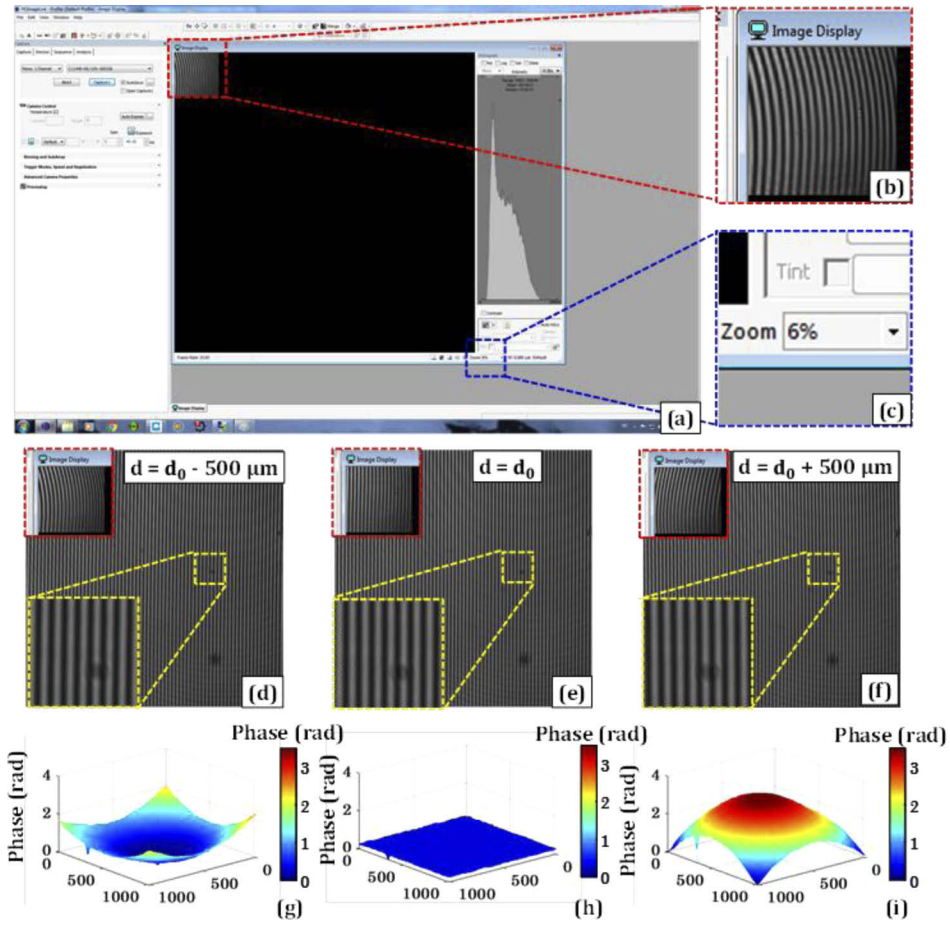

Fig. 5. Experimental study for the sensing of wavefront curvature mismatch using moiré pattern. Two identical objective lenses (10X / 0.25 NA) are used in both object and reference arm. Both reference objective MO_3 and mirror M are translated in order to obtain the condition of mismatched/matched object and reference wavefront curvatures. (a) Screen shots of camera software with demagnified interferograms displayed on a computer screen to demonstrate the moiré fringe formation. The moiré fringes are generated due to the superposition of zoomed out (Magnification 6%) interferograms and computer display's pixels. (b) Zoomed view of the moiré patterns marked with red dotted box shown in Fig. 3(a). Curved moiré fringes depict the curvature mismatch between object and reference beams. (c) Zoomed views of the camera software illustrating zoom (i.e., initial magnification: 6%) of displayed interferograms. Zoom 100% represents the original state of the interferograms. (d – f) Experimental interferograms due to superposition of object and reference beam for the optical path length separation of d_0 – 500 µm, d_0 µm, d_0 + 500 µm, respectively. d_0 is a wavefront curvature matched condition. Insets illustrated in red and yellow color dotted boxes represent corresponding moiré patterns and zoomed interferograms, respectively. (g – i) Reconstructed phase maps obtained from the recorded interferograms are depicted in Figs. 5(d)–5(f). Middle column illustrates the wavefront curvature matched condition between the object and the reference beam. The color maps show phase in radian.

Optics EXPRESS

Next, in order to check the accuracy of the proposed moiré method, the reference arm (MO3 and M) is kept at an arbitrary position, say dZ, from the zero OPD (wavefront curvature match) condition. The reference arm is then moved in a step of 50 μm sequentially to arrive at the wavefront curvature match condition d_0. Figure 6(a) shows the high-density interferogram recorded by the camera and displayed on the monitor. Figure 6(b) shows the zoomed view of the interferogram. It can be seen that the curvature of the fringes from the high-density interferogram or the zoomed in region is difficult to determine. However, when the displayed interferogram is demagnified down to 1%, then the shape of fringes can be easily discerned from the moiré pattern as discussed in the earlier section. Figure 6(c) presents the moiré pattern generated due to the superposition of demagnified interferogram at 1% and array of monitor display's pixels. Figure 6(d) illustrates the recovered phase map corresponding to the interferograms shown in Fig. 6(a). The interferogram, zoomed view of the interferogram, corresponding moiré pattern and phase map for each position of the reference arm displaced by 50 μm can be found in Visualization 2. The straight moiré fringes correspond to almost negligible quadratic phase aberration in the recovered phase images. This would allow performing real-time quantitative phase imaging of biological events at high-temporal resolution without any post processing. Note that the focus of the present method is not the removal of other optical aberrations from the system but only the spherical aberration introduced by the MO. However, the effects of other aberrations can also be observed in the moiré pattern.

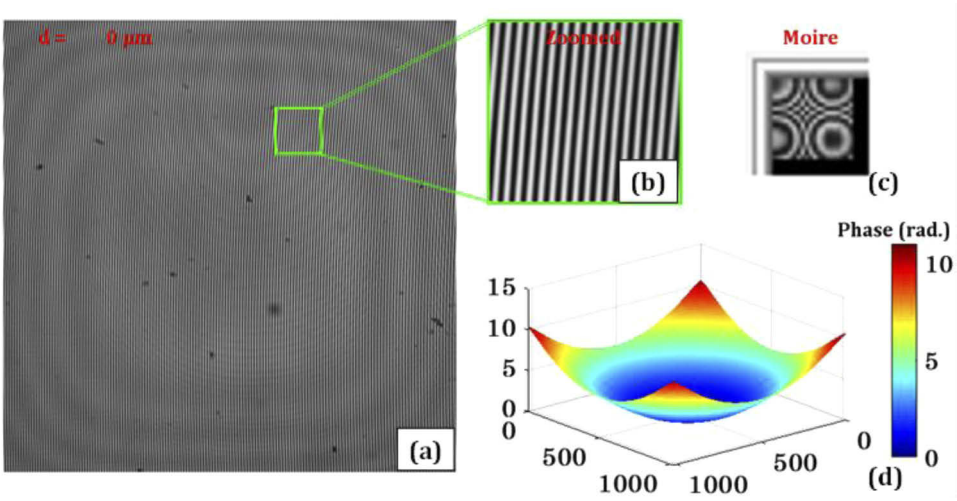

Fig. 6. Wavefront curvature mismatch measurement accuracy. (a) Interferometric image of standard Si wafer corresponding to the random optical path length separation between the object and the reference arm. (b) Zoomed view of the region marked with green solid box. (c) Corresponding moiré fringes generated due to the superposition of zoomed out (magnification 1%) interferogram's and computer display's pixels. (d) Reconstructed phase maps obtained from the recorded interferogram depicted in Fig. 6(a). The color maps show phase in radian. Reference objective MO3 and mirror M both are simultaneously translated in a step of 50 μm in order to obtain the condition of matched object and reference wavefront curvatures (see Visualization 2). The step size of 50 μm is decided by shifting white light interference patterns in a step of 5 μm (see Visualization 1).

Optics EXPRESS

4.3. Effect of wavefront curvature mismatch in the phase imaging of USAF chart and its compensation

To understand the wavefront curvature mismatch measurement accuracy of the moiré method, experiments are further conducted on a USAF resolution chart (R3L3S1N, Negative 1951 USAF chart, Thorlabs). USAF chart is placed under QPM to record interference pattern for different curvature mismatch positions of reference arm at d_0– 500 µm, d_0 µm, d_0 + 500 µm, respectively. Figures 7(a)–7(c) depict the interference patterns of USAF chart for three different positions of the reference arm. The insets marked with red dotted boxes are the zoomed views of small portion of the interference patterns. Figures 7(d)–7(f) illustrate the recovered phase maps corresponding to reference arm positions at d_0– 500 µm, d_0 µm, d_0 + 500 µm. The reference arm position corresponding to d0 represents the flat phase background condition as shown in Fig. 7(e). This position of almost zero quadratic phase aberration is achieved by adjusting the reference arm to achieve straight line moiré fringes. The other two positions at d_0– 500 µm and d_0 + 500 µm represent the wavefront curvature mismatch conditions and generate quadratic phase aberration in the recovered phase images of the resolution chart.

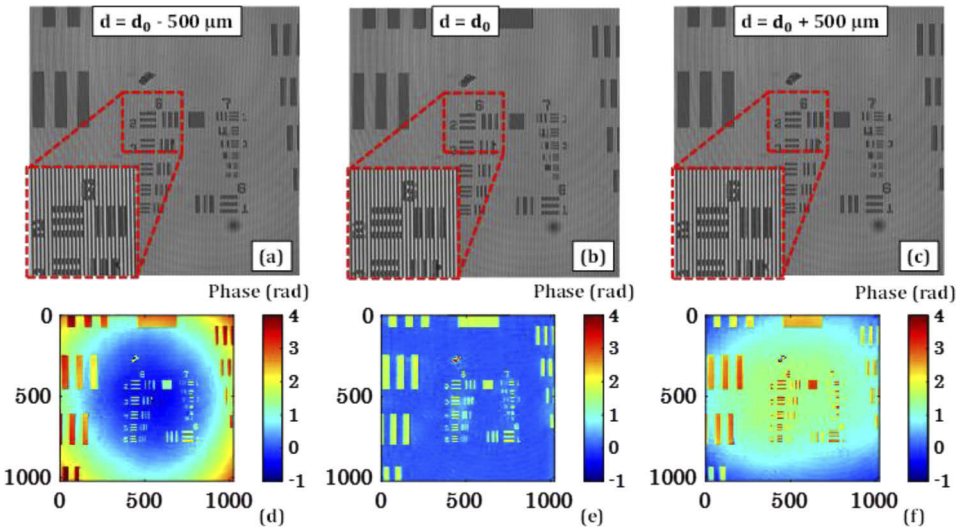

Fig. 7. Wavefront curvature mismatch correction in the phase imaging of USAF chart. 10× (0.25 NA) is being used for the interferometric imaging USAF chart. (a, d) Interferometric images of the resolution chart corresponding to the optical path length separation between the object and the reference arm of d_0– 500 µm, d_0 µm, d_0 + 500 µm, respectively. The insets depict the zoomed view of the region marked with red dotted box. (d – f) Reconstructed phase maps of USAF chart corresponding to the recorded interferograms depicted in Figs. 7(a)–7(c). Middle column illustrates the wavefront curvature matched condition between the object and the reference beam. This condition is obtained by using the concept of moiré pattern presented in Fig. 2. The color maps show phase in radian.

4.4. Comparison of the proposed approach with experimental compensation technique

The accuracy of the proposed technique (sampling moiré pattern) is compared with the experimental compensation technique, i.e., recording an additional sample-free interferogram prior to the sample investigation and simply subtracting both the phase maps. Figures 8(a)–8(d) illustrate the results for the displacement of 1 mm from the curvature matched condition. It can be seen from Fig. 8(c), the reconstructed phase map contains a quadratic phase aberration prior to the experimental compensation technique. This aberration is compensated by simply subtracting the

Optics EXPRESS

phase of the sample free region as shown in Fig. 8(d). Figures 8(e)–8(g) represent the results of the proposed approach based on moiré fringe method. It can be seen from Fig. 8(g) that the proposed approach reconstruct quadratic aberration free phase map of the specimen. The experimental compensation technique has a slight performance edge over the proposed technique. It also removes other optical aberrations, like monochromatic aberrations, caused due to the optical system at the cost of recording two interferograms. However, the proposed approach has an edge like high speed over the experimental compensation technique while dealing with the monochromatic aberration free optical system. The type of the monochromatic aberrations would depend on the quality of the optical components used to develop the phase microscope. If the phase microscope is free from all types of monochromatic aberrations like spherical aberration, astigmatism, coma, field curvature and distortion, then the proposed approach called moiré fringe method will work satisfactorily.

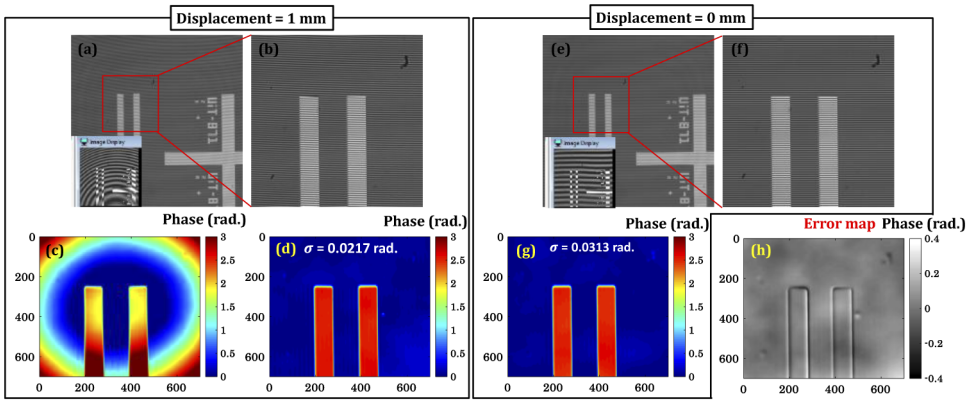

Fig. 8. Comparison of the experimental compensation technique with the proposed approach. (a, b) Interferogram of the optical waveguide and its zoomed region marked with red box at displacement of 1 mm from curvature matched condition. (c, d) Reconstructed phase maps of the zoomed region before and after phase subtraction of the reference interferogram. (e, f) Interferogram of the optical waveguide and its zoomed region marked with red box at displacement of curvature matched condition. The insets in Figs. 8(a) and 8(e) illustrate the moiré patterns. (g) Reconstructed phase map of the zoomed region shown in Fig. 8(f). (h) Error phase map obtained from the subtraction of the reconstructed phase maps using experimental compensation method and moiré method.

In addition, for several applications finding sample-free area might be demanding, such as the target applications, i.e. imaging of pathological tissue sections (see next section) which are usually millimeter to centimeter sized. The standard deviation is found to be equal to 0.0217 and 0.0313 rad corresponding to the experimental compensation technique and proposed approach. Both the results are found to be in a good agreement with each other. The error map obtained from the subtraction of the reconstructed phase maps using physical method and moiré method is shown in the Fig. 8(h). It can be seen that the errors are concentrated on the borders of the bars.

4.5. Wavefront curvature mismatch compensation for non-identical objectives in high resolution phase imaging of tissue sample

For all the experimentation shown in the previous sections, two identical objective lenses (10×/0.25NA) are being used in both the object and the reference arm of QPM system. In order to exhibit the potential of the proposed method, the sample objective (MO_2) is replaced with an objective lens (60×/1.2NA) for high resolution phase imaging of the biological specimens. Note that for non-identical objective lenses in the object and the reference arm, the zero OPD

Optics EXPRESS

position of the reference arm does not correspond to wavefront curvature matched position. This is contrary to the experimental settings in case of identical objectives. The reference arm is then translated to achieve zero quadratic phase aberration condition by observing the shape of moiré fringe patterns. In this section, we also compare the accuracy of the proposed moiré method with a standard numerical method for quadratic phase aberration compensation called principle component analysis (PCA) [20].

First, an interferogram of the tissue sample (thickness ~ 1 μm) is recorded with high NA objective lens with unknown wavefront curvature mismatch between the object and the reference wave. The reference arm of the interferometer is kept at an arbitrary position for interferogram recording of tissue sample as shown in Fig. 9(a). Square shaped fringes present in Figs. 9(a) and 9(d) could be due to imperfection in the camera. When the camera sensor is examined using naked eyes under ceiling light (white light) illumination, these fringes were present in the sensor's active area. This could be due to the imperfect sandwiching of the protecting cover glass on the sensor. This has been further verified experimentally by replacing the camera and observing the disappearance of the square shaped fringes. The reference arm of the interferometer is then translated in a way such that straight moiré fringes are observed in the display of camera acquisition software. The interferogram is displayed at 1% to observe the moiré fringe pattern in

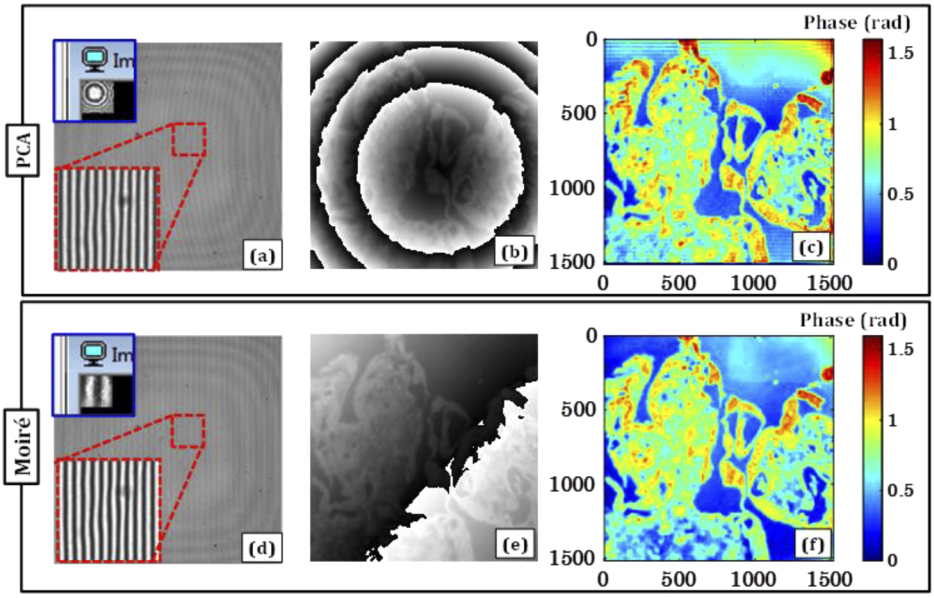

Fig. 9. Wavefront curvature mismatch compensation using Moiré and its comparison with PCA based curvature correction in the phase imaging of biological tissues. 60× (1.2 NA) is being used for the interferometric imaging tissue sample. (a, d) Interferometric images of the biological specimen corresponding to the curvature mismatched and matched between the object and the reference arm. This is done by translating the reference arm assembly (objective lens and mirror). The insets depict the zoomed view of the region marked with red dotted box and Moiré fringes generated due to the superposition of zoomed out (Magnification 1%) interferograms and computer display's pixels. (b, e) Corresponding unwrapped phase maps. (c) Reconstructed phase map of tissue sample using PCA based curvature mismatch correction algorithm corresponding to the recorded interferogram depicted in Fig. 9(a). (f) Reconstructed phase map corresponding to the interferogram depicted in Fig. 9(d). The curvature mismatch is sensed and corrected by employing the concept of Moiré pattern presented in Fig. 1. The color maps show phase in rad.

Optics EXPRESS

the camera software. Figure 9(d) illustrates the interferogram of the same tissue sample when the object and the reference wavefront curvatures are matched by employing the concept of moiré pattern described in the previous section. The insets enclosed in blue color boxes depict the moiré patterns of the interferograms shown in Figs. 9(a) and 9(d).

The interferograms are further post processed using Fourier transform based phase recovery algorithm to obtain their wrapped phase maps depicted in Figs. 9(b) and 9(e), respectively. The wrapped clearly illustrate the presence of quadratic phase aberration in the interferogram shown in Fig. 9(a). In contrast, the quadratic phase aberration is not present in the interferogram depicted in Fig. 9(d) as can be confirmed from its wrapped phase map as well. Figures 9(c) and 9(f) illustrate the recovered phase maps of the tissue sample by employing PCA and Fourier transform based phase retrieval algorithms [9,20]. It can be seen from Fig. 9(c) that PCA based recovery removes the quadratic phase aberration successfully from the phase images; however, it generates some fringing artifacts at the edges of the image. Further, numerical compensation of the quadratic phase aberration would increase some computational loads. On the contrary, Fourier transform based phase recovery, from the interferogram recorded after implementing the proposed method, does not generate such artifacts. In addition, the reconstructed phase map does not suffer from the quadratic phase aberration. To measure the quadratic phase aberration compensation capability of both the approaches, a small tissue free regions of the interferograms are selected. The standard deviations corresponding to PCA and proposed approach are found to be equal to 0.104 rad and 0.035 rad, respectively. It can be seen that the proposed method generates less phase error in the measurement comparative to PCA. Thus, the present method can be employed for accurate and high-throughput QPI of the cells and thin tissues sections.

5. Conclusion

High-speed and high phase sensitivity of QPM is useful when capturing dynamics of cell and sub-cellular organelles; and when combining QPM with other functionalities such as optical trapping [9,11], Raman spectroscopy [12] or fluorescence microscopy [36]. Single shot phase recovery algorithm, i.e., Fourier transform method allows for high-imaging. However, for a lossless reconstruction of the object, the zero and first order peaks in the Fourier domain are to be well separated, which mandates a high density of fringes. High fringe density creates problem in discerning the shape of the fringes over the whole FoV of the camera due to the resolution limitation of the human eyes. Moreover, for a faithful and a fast phase reconstruction, the shape and the density of the fringes in the interferograms should be straight and satisfy the Nyquist sampling criteria, respectively. To overcome these limitations, we proposed a new method called sampling moiré method to visualize the shape of the fringe pattern over the entire FoV of the camera. Moiré fringe pattern, which is a low frequency signal compared to the original interferometric images, helps to clearly visualize the shape of the fringe pattern prior to the data acquisition. The interferogram is displayed in the camera acquisition software at lower magnification to identify and correct the shape of the fringes. The proposed method is a simple and real-time physical technique for the quadratic phase aberration compensation. The applicability of the method is demonstrated by performing QPI of USAF resolution chat and 1 μm thick tissue sample.

The proposed sampling moiré method enables high-throughput QPM. In microscopy, high-throughput refers delivering imaging of large number of objects (cells or tissues) over large FoV (areas) in a minimal time. In the proposed approach, quadratic phase distortion is corrected from the entire FoV in a single step, without acquiring multiple images or a need of numerical post-processing, thereby reducing both the acquisition time and the post-processing time. Contrary to other methods based on background removal, the proposed approach is also suitable for applications such as high cell-density and tissue imaging where sample can be present over the entire FoV. Although, present implementation of the method is based on the visual judgement

Optics EXPRESS

criteria, the entire process can be automated i.e. procedure of under-sampling the image can be programmed for the removal of quadratic phase distortion.

The method is not only limited to the current experimental setup. It can be easily implemented with any QPM system for quadratic phase aberration compensation. The proposed method is a physical quadratic phase compensation technique. Therefore, it can be used with those QPM configurations, like, Michelson and Mach Zehnder type etc., where the optical path length of either an object or a reference arm can be adjusted. The optical path length can be changed either by mechanically translating the optical component or by using a tunable lens and electrically controlling the wavefront curvature of the object or the reference fields. The proposed method will also work for multiple wavelengths used simultaneously in QPM system, provided the optical microscopy system used does not have any chromatic aberration and it can be used to generate straight fringes for multiple wavelengths for curvature matched conditions, i.e. when the zero optical path length condition is satisfied.

Funding

H2020 Marie Skłodowska-Curie Actions (MSCA_ITN: 31147); Norges Forskningsråd (NANO 2021: 288565); Norges Forskningsråd (BIOTEK-2021: 285571); Direktoratet for internasjonalisering og kvalitetsutvikling i høgare utdanning (INCP- 2014/10024); The publication charges for this article have been funded by a grant from the publication fund of Universitetet i Tromsø.

Acknowledgements

The authors would like to acknowledge Prof. Purusotam Basnet and Dr. Mona Nystad for providing tissue samples.

Disclosures

The authors declare no conflicts of interest.

References

1. G. Popescu, *Quantitative phase imaging of cells and tissues* (McGraw Hill Professional, 2011).
2. S. Sridharan, V. Macias, K. Tangella, J. Melamed, E. Dube, M. X. Kong, A. Kajdacsy-Balla, and G. Popescu, "Prediction of prostate cancer recurrence using quantitative phase imaging: Validation on a general population," Sci. Rep. **6**(1), 33818 (2016).
3. T. Zhang and I. Yamaguchi, "Three-dimensional microscopy with phase-shifting digital holography," Opt. Lett. **23**(15), 1221–1223 (1998).
4. A. Ahmad, V. Dubey, G. Singh, V. Singh, and D. S. Mehta, "Quantitative phase imaging of biological cells using spatially low and temporally high coherent light source," Opt. Lett. **41**(7), 1554–1557 (2016).
5. V. Dubey, V. Singh, A. Ahmad, G. Singh, and D. S. Mehta, "White light phase shifting interferometry and color fringe analysis for the detection of contaminants in water," in *European Conference on Biomedical Optics*, (Proc. SPIE, 2016), 97181F.
6. K. Creath, "V phase-measurement interferometry techniques," in *Prog. Opt.* (Elsevier, 1988), pp. 349–393.
7. A. Ahmad, A. Kumar, V. Dubey, A. Butola, B. S. Ahluwalia, and D. S. Mehta, "Characterization of color cross-talk of CCD detectors and its influence in multispectral quantitative phase imaging," Opt. Express **27**(4), 4572–4589 (2019).
8. M. Takeda, H. Ina, and S. Kobayashi, "Fourier-transform method of fringe-pattern analysis for computer-based topography and interferometry," J. Opt. Soc. Am. A **72**(1), 156–160 (1982).
9. A. Ahmad, V. Dubey, V. R. Singh, J.-C. Tinguely, C. I. Øie, D. L. Wolfson, D. S. Mehta, P. T. So, and B. S. Ahluwalia, "Quantitative phase microscopy of red blood cells during planar trapping and propulsion," Lab Chip **18**(19), 3025–3036 (2018).
10. A. Ahmad, T. Mahanty, V. Dubey, A. Butola, B. S. Ahluwalia, and D. S. Mehta, "Effect on the longitudinal coherence properties of a pseudothermal light source as a function of source size and temporal coherence," Opt. Lett. **44**(7), 1817–1820 (2019).
11. B. S. Ahluwalia, P. Løvhaugen, and O. G. Hellesø, "Waveguide trapping of hollow glass spheres," Opt. Lett. **36**(17), 3347–3349 (2011).
12. P. Løvhaugen, B. S. Ahluwalia, T. R. Huser, and O. G. Hellesø, "Serial Raman spectroscopy of particles trapped on a waveguide," Opt. Express **21**(3), 2964–2970 (2013).

Optics EXPRESS

13. Y. Liu, Z. Wang, and J. Huang, "Recent progress on aberration compensation and coherent noise suppression in digital holography," Appl. Sci. **8**(3), 444 (2018).
14. Q. Weijuan, Y. Yingjie, C. O. Choo, and A. Asundi, "Digital holographic microscopy with physical phase compensation," Opt. Lett. **34**(8), 1276–1278 (2009).
15. W. Zhou, Y. Yu, and A. Asundi, "Study on aberration suppressing methods in digital micro-holography," Opt. Lasers Eng. **47**(2), 264–270 (2009).
16. A. Doblas, E. Sánchez-Ortiga, M. Martínez-Corral, G. Saavedra, P. Andrés, and J. Garcia-Sucerquia, "Shift-variant digital holographic microscopy: inaccuracies in quantitative phase imaging," Opt. Lett. **38**(8), 1352–1354 (2013).
17. A. Doblas, D. Hincapie-Zuluaga, G. Saavedra, M. Martínez-Corral, and J. Garcia-Sucerquia, "Physical compensation of phase curvature in digital holographic microscopy by use of programmable liquid lens," Appl. Opt. **54**(16), 5229–5233 (2015).
18. P. Ferraro, S. De Nicola, A. Finizio, G. Coppola, S. Grilli, C. Magro, and G. Pierattini, "Compensation of the inherent wave front curvature in digital holographic coherent microscopy for quantitative phase-contrast imaging," Appl. Opt. **42**(11), 1938–1946 (2003).
19. L. Miccio, D. Alfieri, S. Grilli, P. Ferraro, A. Finizio, L. De Petrocellis, and S. Nicola, "Direct full compensation of the aberrations in quantitative phase microscopy of thin objects by a single digital hologram," Appl. Phys. Lett. **90**(4), 041104 (2007).
20. C. Zuo, Q. Chen, W. Qu, and A. Asundi, "Phase aberration compensation in digital holographic microscopy based on principal component analysis," Opt. Lett. **38**(10), 1724–1726 (2013).
21. J. Sun, Q. Chen, Y. Zhang, and C. Zuo, "Optimal principal component analysis-based numerical phase aberration compensation method for digital holography," Opt. Lett. **41**(6), 1293–1296 (2016).
22. J. Di, J. Zhao, W. Sun, H. Jiang, and X. Yan, "Phase aberration compensation of digital holographic microscopy based on least squares surface fitting," Opt. Commun. **282**(19), 3873–3877 (2009).
23. H. Yu, S. Jia, J. Dong, D. Huang, and S. Xu, "Phase curvature compensation in digital holographic microscopy based on phase gradient fitting and optimization," J. Opt. Soc. Am. A **36**(12), D1–D6 (2019).
24. T. Nguyen, V. Bui, V. Lam, C. B. Raub, L.-C. Chang, and G. Nehmetallah, "Automatic phase aberration compensation for digital holographic microscopy based on deep learning background detection," Opt. Express **25**(13), 15043–15057 (2017).
25. K. Khare, *Fourier optics and computational imaging* (John Wiley & Sons, 2015).
26. I. Amidror, "Sub-Nyquist artefacts and sampling moiré effects," R. Soc. Open Sci. **2**(3), 140550 (2015).
27. K. Patorski, *Handbook of the moiré fringe technique* (Elsevier Science, 1993).
28. S. Yokozeki, K. Patorski, and K. Ohnishi, "Collimation method using Fourier imaging and moiré techniques," Opt. Commun. **14**(4), 401–405 (1975).
29. F. J. Torcal-Milla and L. M. Sanchez-Brea, "Collimation technique and testing applied to finite size polychromatic sources," Appl. Opt. **56**(12), 3628–3633 (2017).
30. S. Ri, S. Hayashi, S. Ogihara, and H. Tsuda, "Accurate full-field optical displacement measurement technique using a digital camera and repeated patterns," Opt. Express **22**(8), 9693–9706 (2014).
31. C. Li, Z. Liu, H. Xie, and D. Wu, "Novel 3D SEM Moiré method for micro height measurement," Opt. Express **21**(13), 15734–15746 (2013).
32. K. Patorski, M. Wielgus, M. Ekielski, and P. Kaźmierczak, "AFM nanomoiré technique with phase multiplication," Meas. Sci. Technol. **24**(3), 035402 (2013).
33. J. W. Goodman, *Speckle phenomena in optics: theory and applications* (Roberts and Company Publishers, 2007).
34. A. Ahmad, V. Dubey, V. Singh, A. Butola, T. Joshi, and D. S. Mehta, "Reduction of spatial phase noise in the laser based digital holographic microscopy for the quantitative phase measurement of biological cells," in *European Conference on Biomedical Optics*, (Proc. SPIE 2017), 104140H.
35. V. Dubey, D. Popova, A. Ahmad, G. Acharya, P. Basnet, D. S. Mehta, and B. S. Ahluwalia, "Partially spatially coherent digital holographic microscopy and machine learning for quantitative analysis of human spermatozoa under oxidative stress condition," Sci. Rep. **9**(1), 1–10 (2019).
36. V. Dubey, A. Ahmad, R. Singh, D. L. Wolfson, P. Basnet, G. Acharya, D. S. Mehta, and B. S. Ahluwalia, "Multi-modal chip-based fluorescence and quantitative phase microscopy for studying inflammation in macrophages," Opt. Express **26**(16), 19864–19876 (2018).